Journal of Materials Chemistry A

ROYAL SOCIETY OF CHEMISTRY

PAPER

View Article Online
View Journal | View Issue

Cite this: J. Mater. Chem. A, 2026, 14, 4268

Nb doping strategy for active site modification in Co_3O_4 to enable concurrent hydrogen production and glycerol valorization for efficient formate production

Shobharajsinh Rathod, Kinjal K. Joshi, Pratik M. Pataniya, C. K. Sumesh and Sanni Kapatel *

The electrocatalytic glycerol oxidation reaction (GOR) has emerged as a sustainable and energy-efficient alternative to the oxygen evolution reaction (OER), offering the dual advantage of hydrogen (H_2) generation through the hydrogen evolution reaction (HER) and selective upgrading of biomass-derived glycerol into value-added chemicals like formate. However, to address the contemporary challenge of developing low-cost and stable electrocatalysts for the GOR we have synthesized a niobium-doped cobalt oxide (Nb-Co_3O_4) based electrode with a binder-free approach. Herein, we report Nb–Co_3O architecture (designated as 3NCO for 3% doping of Nb) on nickel foam (NF) *via* a hydrothermal strategy, serving as a high-performance, bifunctional electrocatalyst for the HER, OER, and GOR. Nb incorporation into the Co_3O_4 lattice, evidenced by XRD peak shifts, Raman mode alterations, and XPS valence changes, introduces lattice distortion and electronic modulation, and FESEM morphological advancements, which collectively enhance active site density and charge transfer kinetics under alkaline conditions. As a result, the 3NCO/NF electrode exhibits excellent activity, requiring only 196 mV overpotential to achieve 10 mA cm^{-2} for the HER, and 1.50 V *vs.* RHE for the OER in 1 M KOH. Notably, in 0.1 M glycerol + 1 M KOH, the GOR proceeds at just 1.19 V *vs.* RHE, achieving a remarkable potential drop of 330 mV compared to the OER, and enabling overall electrolysis at 1.46 V in a two-electrode system. This work highlights the role of lattice Nb doping in boosting active site availability and electron transfer, positioning 3NCO/NF as a robust platform, by sustaining more than 90% of faradaic efficiency, for energy-saving H_2 production and electrochemical glycerol valorization.

Received 16th October 2025
Accepted 29th November 2025

DOI: 10.1039/d5ta08434b

rsc.li/materials-a

1. Introduction

Hydrogen energy is an eco-friendly and valuable energy carrier with the potential to achieve carbon neutrality, address energy crises, and protect the environment. Unlike traditional hydrogen production methods such as fossil fuel-based processes, steam methane reforming, and industrial byproduct extraction, water electrolysis has gained attention for its lower environmental impact and ability to produce high-purity hydrogen.[1] The development of electrocatalytic water-splitting technology is largely constrained by the high energy demand of the Oxygen Evolution Reaction (OER). Despite the theoretical minimum potential of 1.23 V, even the most advanced catalysts fail to operate below this limit.[2,3] To address this challenge, an effective strategy involves replacing the OER with the oxidation of organic molecules that have lower oxidation potentials, thereby reducing overall energy consumption and enhancing hydrogen production efficiency. Recent research has explored various easily oxidizable compounds, including hydrazine, urea, glycerol, methanol, ethanol, isopropanol, and ethylene glycol, as alternatives at the anode.[4] While these molecules can significantly decrease the energy input required for water splitting, their widespread adoption is hindered by their high cost.[5,6]

In this context, glycerol, an abundant and low-cost byproduct of biodiesel production, emerges as an ideal anode reactant for electrochemical applications. Due to its high accessibility and low cost, glycerol is an important bio-derived material for the anodic oxidation process.[7] It can be efficiently converted into valuable chemicals, including glycolic acid, oxalic acid, formic acid, and glyceric acid. Particularly, formic acid is an attractive product due to its low toxicity, ease of availability, and role as a hydrogen storage carrier in direct formic acid fuel cells.[8] Replacing the oxygen evolution reaction (OER) with the more favourable glycerol electrooxidation reaction (GOR), the overpotential required for hydrogen production can be significantly

Department of Physical Sciences, P D Patel Institute of Applied Sciences, Charotar University of Science and Technology, CHARUSAT, Changa-388 421, Gujarat, India. E-mail: sannikapatel.phys@charusat.ac.in

reduced, thereby improving overall energy conversion efficiency.

However, the widespread adoption of the GOR is limited by the high cost and selectivity concerns of noble metal (*e.g.*, platinum, iridium, rhodium, palladium, ruthenium, *etc.*) based catalysts. Therefore, there is a need for the development of low-priced, highly selective alternative catalysts. In recent years, cobalt oxides have garnered significant interest as promising candidates for the OER and GOR due to their relatively stable structure and high intrinsic activity. Their flexible composition, featuring a tuneable Co^{2+}/Co^{3+} redox pair, allows for further optimization of catalytic performance.[9] Additionally, the simple fabrication methods for cobalt oxides enable additional customization of their properties, which can significantly enhance their catalytic effectiveness.[10,11] The incorporation of single atoms into Co_3O_4 significantly improves its catalytic efficiency for the HER, OER, and alcohol oxidation reactions.[12] This enhancement stems from the introduction of highly active, isolated catalytic sites that adjust the electronic structure, accelerate reaction kinetics, and increase the density of active sites.[13,14] These modifications collectively elevate catalytic activity, selectivity, and durability. Notably, embedding single atoms within spinel structures has emerged as a promising approach for boosting electro-oxidation performance.[15] Moreover, the integration of niobium (Nb) into cobalt-based materials has emerged as a highly effective approach for improving electrochemical activity. Nb, with its high oxidation state (Nb^{5+}) and strong ability to modulate the electronic structure, promotes the formation of oxygen vacancies, enhances electrical conductivity, and accelerates charge transfer processes.[16,17] Furthermore, Nb doping significantly perpetuates structural stability under harsh electrochemical conditions, ensuring greater catalyst resilience and maintaining high selectivity during prolonged operation. These synergistic effects make Nb atom a powerful dopant for advancing both electro-oxidation and hydrogen evolution reactions. For example, Wang *et al.* demonstrated a catalyst design strategy by doping single-atom Bi into the spinel oxide structure of Co_3O_4, significantly enhancing the GOR towards formate production. In addition, both experimental and theoretical studies revealed that Bi single atoms at Co_{Oh}^{3+} sites promote Co_{Td}^{2+} oxidation, increasing OH* generation, which is crucial for catalyzing the oxidation of hydroxyl groups and C–C bond cleavage in glycerol.[18] Furthermore, Zhu *et al.* reported that incorporating iridium (Ir) single atoms into cobalt oxide (Co_3O_4) enhances the oxygen evolution reaction (OER) under acidic conditions.[19] In this study, the Ir and Co atoms, with bridged electrophilic oxygen ligands, act as active sites, improving electronic conductivity and lowering the energy barrier, outperforming IrO_2 catalysts. Gao *et al.* developed a Ru-Co_3O_4 catalyst for hydrazine oxidation, demonstrating superior electrochemical performance with a low onset potential of −0.15 V *vs.* RHE.[20] The catalyst's design enhances active site utilization and stability, enabling efficient energy conversion in direct hydrazine fuel cells.

In this work, we present a systematic investigation of a Nb-doped Co_3O_4 electrocatalyst supported on nickel foam for hybrid water electrolysis and glycerol electrooxidation. The catalyst was synthesized *via* a one-step *in situ* hydrothermal method and characterized using various techniques such as XRD, XPS, HRTEM, FESEM, and EDX techniques to confirm successful Nb incorporation into the Co_3O_4 lattice and its impact on the electronic structure. The electrocatalytic performance of the Nb-Co_3O_4/NF electrode was evaluated for the hydrogen evolution reaction (HER), oxygen evolution reaction (OER), and glycerol oxidation reaction (GOR) using linear sweep voltammetry (LSV), electrochemical impedance spectroscopy (EIS), and chronoamperometry. With the addition of glycerol to the electrolyte, the electrode displayed enhanced current densities at significantly reduced overpotentials, indicating a strong promotional effect of glycerol on electrochemical performance. HPLC analysis confirmed formate as the major oxidation product, underscoring the dual functionality of the system for hydrogen and value-added chemical production. The electrode demonstrated remarkable stability over prolonged operation and achieved low cell voltages at industrially relevant current densities. An Nb-doping strategy was employed to tune the electronic structure of Co_3O_4, enhancing OH* intermediate formation and boosting both glycerol oxidation and hydrogen evolution. The resulting catalyst achieves concurrent hydrogen generation and selective glycerol-to-formate conversion with outstanding durability, advancing a sustainable pathway for clean energy production. To our knowledge, this is among the first reports on Nb-doped Co_3O_4 for glycerol-assisted electrolysis, offering insights into the design of low-cost, non-noble metal-based catalysts for energy-efficient hydrogen and formate co-generation.

2. Experimental

2.1 Chemicals

Cobalt(II) chloride hexahydrate {$CoCl_2 \cdot 6(H_2O)$}, (AR, 99%), ammonium fluoride {NH_4F} (AR, 98%), urea {$CO(NH_2)_2$} (AR, 99%) and niobium(V) chloride {$NbCl_5$} (AR, 99%) were purchased from Merck Life Science Private Ltd. Potassium hydroxide {KOH} (AR, 85%) was purchased from Sisco research laboratories Pvt Ltd. Glycerol {$C_3H_8O_3$} (AR, 99.5%) was purchased from Loba Chemie Pvt Ltd. All of these chemicals were used as received. Nickel foam (NF) was obtained from Vritra Technologies. Silver/silver chloride {Ag/AgCl} electrodes were obtained from Metrohm.

2.2 Procedure of electrode fabrication

The 3% niobium-doped cobalt oxide (3NCO/NF) electrode was synthesized using a hydrothermal method. To prepare the precursor solution, 9.7 mmol of cobalt(II) chloride hexahydrate ($CoCl_2 \cdot 6H_2O$) and 0.3 mmol of niobium(V) chloride ($NbCl_5$) were dissolved in 30 mL of deionized water, along with 30 mmol of urea ($CO(NH_2)_2$) and 75 mmol of ammonium fluoride (NH_4F). Urea served as a slow-release source of hydroxyl (OH^-) and carbonate (CO_3^{2-}) ions, which promoted the controlled precipitation of Co–Nb hydroxide species, while NH_4F released fluoride (F^-) ions that acted as morphology-directing agents by

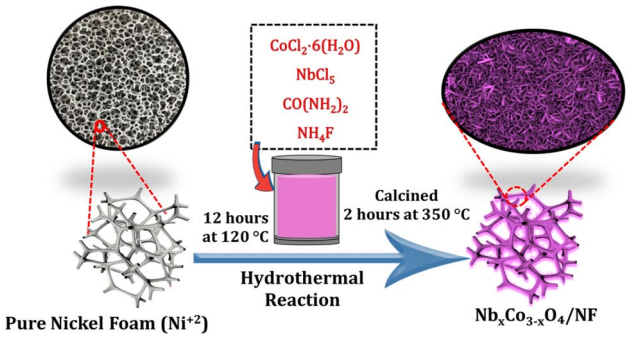

Fig. 1 Hydrothermal synthesis of $Nb_xCo_{3-x}O_4$/NF.

selectively adsorbing on crystal planes and guiding the anisotropic growth of nanostructures on NF. The mixture was stirred magnetically for 15 minutes to ensure homogeneity. The resulting solution was then transferred into a 100 mL Teflon-lined stainless-steel autoclave containing a pre-treated (SN 1) nickel foam (NF) substrate. The autoclave was sealed and maintained at 120 °C for 12 hours to promote hydrothermal growth of the precursor material. After naturally cooling to room temperature, the obtained Nb-$Co(OH)_2$/NF composite was thoroughly washed with deionized water and acetone, followed by drying at 60 °C for 6 hours. Subsequently, the dried sample was calcined in air at 350 °C for 2 hours in a tube furnace, forming crystalline 3NCO/NF. Pristine Co_3O_4/NF was synthesized using the same hydrothermal method, excluding the niobium precursor. For comparison, Nb-doped samples with 1%, 2%, and 3% doping levels were prepared by adjusting the stoichiometric ratios of the metal precursors to obtain Nb_x-$Co_{3-x}O_4$/NF electrodes and characterized using various physicochemical techniques (SN 2) (Fig. 1).

2.3 Electrochemical performance

The electrochemical performance of the binder-free catalytic electrodes toward the hydrogen evolution reaction (HER), oxygen evolution reaction (OER), and glycerol oxidation reaction (GOR) was evaluated using an Autolab/PGSTAT-M204 electrochemical workstation (Metrohm). All measurements were performed at room temperature in a standard three-electrode configuration, with the prepared electrode as the working electrode, platinum (Pt) wire as the counter electrode, and a saturated Ag/AgCl electrode as the reference. The electrodes were immersed in 50 mL of 1 M KOH, with and without the addition of 0.1 M glycerol as the electrolyte. Linear sweep voltammetry (LSV) for the HER was conducted at a scan rate of 5 mV s^{-1} and measured potentials were converted to the reversible hydrogen electrode (RHE) scale using the relationship: $E_{RHE} = E_{AgCl/Ag} + 0.1976 + \{0.059 \times pH\}$ (V). The overpotential (η) was determined as: $(\eta) = -E$ (V *vs.* RHE). Tafel slopes were obtained by fitting the linear regions of the Tafel equation: $\eta = b\log|J| + a$ (here J stands for current density in LSV). Electrochemical impedance spectroscopy (EIS) was carried out over a frequency range of 0.01 Hz to 1 MHz to analyze the charge-transfer resistance. Cyclic voltammetry (CV) was performed within the non-faradaic potential region at scan rates of 10–100 mV s^{-1} to determine the electrochemical double-layer capacitance (C_{dl}). C_{dl} was extracted from the slope of the plot of capacitive current density ($\Delta J/2 = (J_{anodic} - J_{cathodic})/2$) *vs.* scan rate, providing an indirect estimate of the electrochemically active surface area (ECSA). To assess the intrinsic activity of the catalysts, the turnover frequency (TOF) was calculated using the expression $TOF = (j \times A)/(2 \times F \times n)$, where j denotes the current density, A the electrode area, F the Faraday constant, and n the number of active sites involved in the reaction. The factor of 2 corresponds to the number of electrons transferred per H_2 molecule evolved during the HER. Chronopotentiometry was employed to evaluate the long-term stability of the catalysts under HER conditions.

To further assess practical electrolytic performance for hydrogen and formate co-production, a single-compartment electrolyzer was assembled using a symmetric 3NCO/NF‖3NCO/NF configuration, with electrodes positioned 1 cm apart and immersed in 50 mL of 1 M KOH + 0.1 M glycerol. For comparison, conventional alkaline water electrolysis was performed in 1 M KOH under identical conditions. Polarization curves and five consecutive chronoamperometric cycles at fixed potentials were recorded in a two-electrode configuration. After 12 hours of glycerol electrolysis, electrolyte samples were collected for product identification and quantification (SN 3 & 4).

3. Results and discussion

3.1 Physical characterization

Fig. 2A presents the X-ray diffraction (XRD) analysis of the Nb-doped Co_3O_4/NF (NCO/NF) electrode, where the diffraction patterns show prominent peaks corresponding to the spinel Co_3O_4 phase (JCPDS #09-0418), confirming the successful synthesis of the material without the presence of any other impure phase. Notably, a shift of the diffraction peaks towards higher 2θ values is observed with increasing Nb content, indicating the successful incorporation of Nb into the Co_3O_4 lattice *via* substitutional doping.[21] This shift is attributed to the smaller ionic radius of Nb^{5+} (0.69 Å) compared to Co^{2+} (0.72 Å) ions, resulting in a reduction of the lattice spacing and, consequently, a contraction of the lattice. Specifically, the (311) diffraction peak, which is the characteristic peak of the Co_3O_4 phase, shifts from $2\theta = 37.23°$ for the pristine Co_3O_4/NF to 37.90° upon Nb incorporation. The change in lattice spacing (d) can be quantified using Bragg's law, where the initial d-spacing of 2.41 Å decreases to 2.37 Å upon Nb doping, resulting in a contraction of approximately 0.041 Å. This decrease in the d-spacing further confirms the lattice contraction due to Nb^{5+} substitution. The incorporation of Nb is substantiated by the absence of additional diffraction peaks corresponding to niobium oxides (Nb_2O_5), suggesting that Nb is uniformly integrated into the Co_3O_4 lattice or possibly exists in an amorphous phase. Moreover, the diffraction spectra display distinct peaks of the NF substrate, corresponding to the (111) and (200) planes of the cubic nickel structure (PDF #04-0850) at 2θ values of 44.5° and 51.8°, respectively. These peaks can be clearly identified

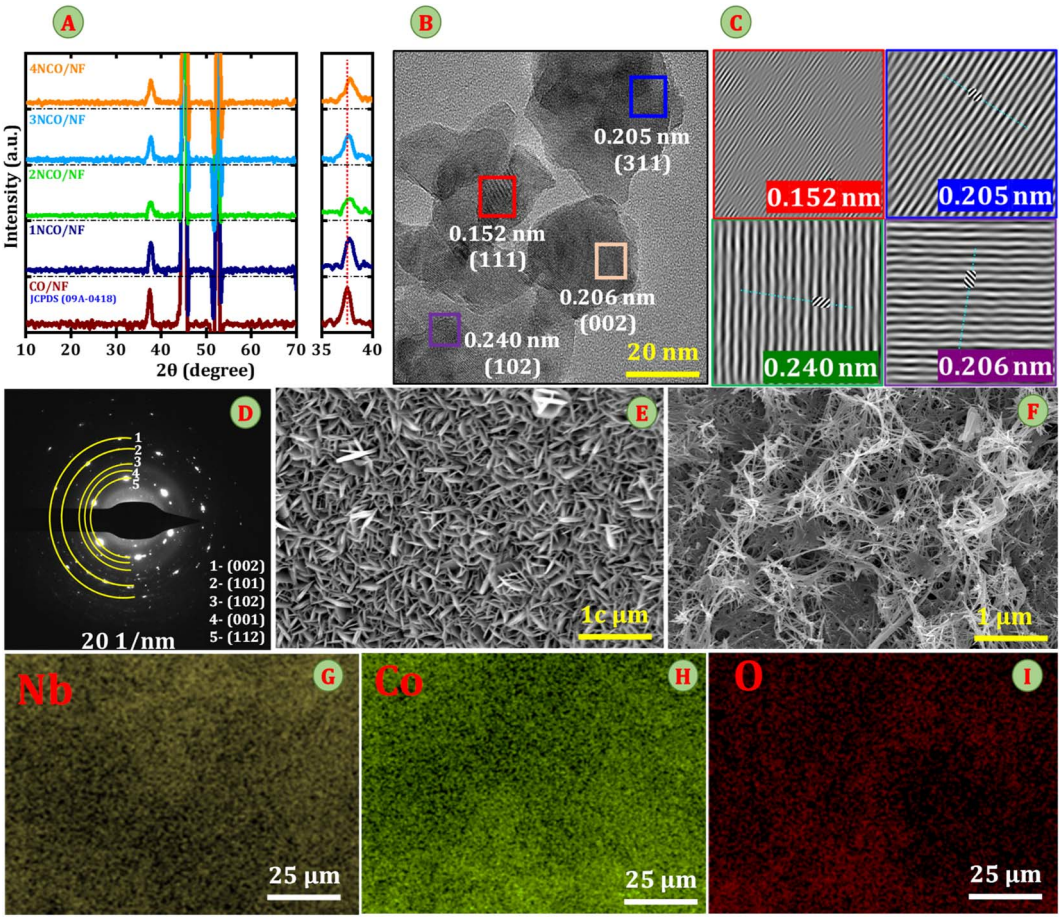

Fig. 2 (A) XRD patterns of CO/NF, 1NCO/NF, 2NCO/NF, 3NCO/NF, and 4NCO/NF; (B) high-resolution transmission electron microscopy (HRTEM) image; (C) inverse fast Fourier transform (iFFT) lattice analysis; (D) selected area electron diffraction (SAED) pattern; (E) field-emission scanning electron microscopy (FESEM) image of pristine CO/NF; (F) FESEM image of 3NCO/NF; and (G–I) elemental mapping images of Co, Nb, and O in 3NCO/NF.

and serve as a reference for distinguishing the NF substrate from the Co_3O_4 peaks. It is expected that Nb doping, along with enhanced structural integrity, will improve electrochemical performance by facilitating more efficient charge transfer, reducing resistance, and increasing the density of catalytically active sites, thereby boosting the overall efficiency of water splitting.[22]

To validate the crystal structure of the Nb-doped Co_3O_4/NF catalyst, high-resolution transmission electron microscopy (HRTEM) was utilized, as shown in Fig. 2B. The corresponding inverse Fast Fourier Transform (iFFT) analysis (Fig. 2C) reveals distinct lattice fringes with interplanar spacings of 0.260 nm, 0.205 nm, 0.206 nm, and 0.240 nm, indexed to the (101), (002), (111), and (311) crystal planes of Co_3O_4/NF, respectively. These values confirm the high crystallinity and structural integrity of the Nb-doped Co_3O_4 nanosheets. The selected area electron diffraction (SAED) pattern in Fig. 2D further shows concentric diffraction rings indexed at (002), (101), (102), (001), and (112), which are consistent with JCDPS 09-0418, revealing polycrystalline property, and confirming successful Nb incorporation into the Co_3O_4 lattice. The surface morphology of both the pristine Co_3O_4 and Nb-doped Co_3O_4 (3NCO/NF) catalysts was investigated using field emission scanning electron microscopy (FESEM). The FESEM image of pristine Co_3O_4 (Fig. 2E) shows vertically aligned nanosheets uniformly grown on the nickel foam substrate. These nanosheet structures, formed *via* a hydrothermal reaction, exhibit open and porous architecture, with exposed edges contributing to a moderately high surface area.[23] In contrast, the incorporation of Nb into the Co_3O_4 lattice results in a notable morphological transformation. Fig. 2F shows that the 3NCO/NF catalyst forms a densely interconnected network of vertically aligned nanowires uniformly covering the nickel foam. This transition from nanosheets to one-dimensional nanowire structures is attributed to the influence of Nb^{5+} ions, which modulate nucleation and crystal growth during the hydrothermal synthesis. Niobium likely serves as a structure-directing agent, promoting anisotropic growth and enhancing crystallinity in the Co_3O_4 phase. This structural evolution increases the number of accessible electroactive sites and improves electrical connectivity among the nanowires.[24] Fig. 2G–I presents the elemental mapping of the 3NCO/NF catalyst, highlighting the uniform spatial distribution of Nb, Co, and O elements across the nickel foam substrate. This homogeneity confirms the successful

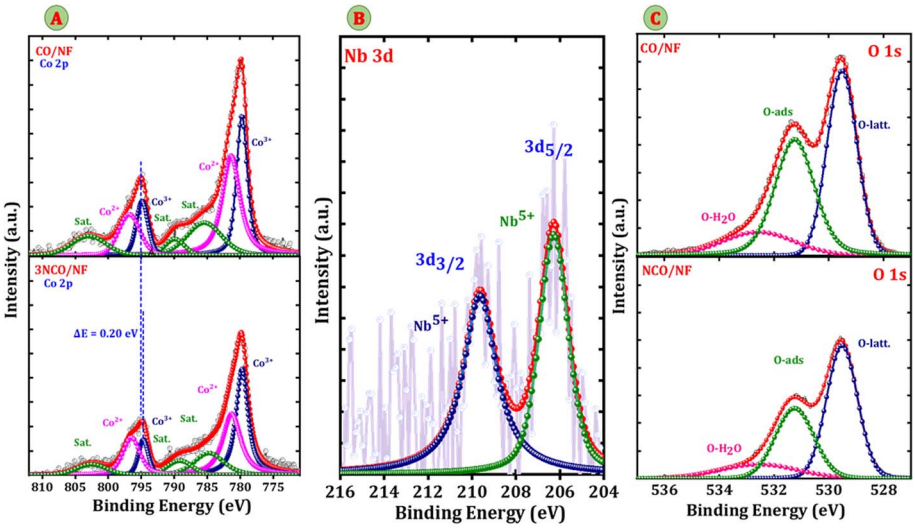

Fig. 3 XPS spectra of pristine Co_3O_4 and 3NCO/NF: (A) Co 2p, (B) Nb 3d, and (C) O 1s, showing the binding energy and chemical states of Co, Nb, and O in the Nb-doped Co_3O_4/NF catalyst.

integration of niobium into the Co_3O_4 framework without phase segregation. Complementary energy-dispersive X-ray spectroscopy (EDS) (Fig. S1) further corroborates the elemental composition and distribution, revealing the presence of Nb, Co, and O, with corresponding weight percentages of 1.30%, 39.80%, and 58.70%, respectively. These findings affirm the uniform integration of Nb and Co throughout the 3NCO/NF catalyst, with oxygen consistently distributed, thus supporting the formation of a well-defined and chemically homogeneous Nb-Co_3O_4 phase.

Furthermore, X-ray photoelectron spectroscopy (XPS) was performed to investigate the surface composition and electronic states of Co, Nb, and O in pristine CO/NF and electrodes. The survey spectra (Fig. S2) confirm the successful incorporation of Nb into the 3NCO/NF structure, as evidenced by the presence of characteristic Nb signals. The Co 2p spectrum reveals two distinct spin–orbit doublets, corresponding to Co^{3+} and Co^{2+}, along with characteristic satellite peaks indicative of multiplet splitting. The binding energies of Co^{3+} are observed at 779.69 eV (Co $2p_{3/2}$) and 794.50 eV (Co $2p_{1/2}$), while those of Co^{2+} appear at 781.33 eV (Co $2p_{3/2}$) and 796.54 eV (Co $2p_{1/2}$), with an additional satellite peak at 802.84 eV. A notable negative shift in the Co 2p binding energies upon Nb doping (Fig. 3A) suggests an increase in electron density at Co sites, likely due to electron transfer from Nb to Co, which alters the local electronic environment and enhances metal–ligand interactions. Furthermore, the observed decrease in Co^{3+} peak intensity upon Nb^{5+} doping suggests a subtle perturbation of the Co^{3+} sites, likely due to electron redistribution and modification of the local coordination environment. This indicates that Nb incorporation affects the electronic structure and may influence the relative population of Co oxidation states within the spinel lattice.[25] This charge redistribution significantly improves electrical conductivity, lowers charge-transfer resistance, and facilitates electrocatalytic reactions during the HER, OER, and GOR, thereby enhancing overall catalytic efficiency. Furthermore, Nb doping optimized electronic structure of Co_3O_4 for the glycerol oxidation reaction (GOR) by increasing electron density at Co sites, which strengthens hydroxyl (OH) adsorption*, lowers the oxidation overpotential, accelerates electron transfer kinetics, and stabilizes active oxygen species, ultimately improving reaction efficiency.[26] The Nb 3d spectrum (Fig. 3B) exhibits two peaks at 207.3 eV and 210.5 eV, corresponding to Nb $3d_{5/2}$ and Nb $3d_{3/2}$, confirming the presence of Nb^{5+} oxidation state and its successful incorporation into the Co_3O_4/NF structure. Additionally, the deconvoluted O 1s spectrum (Fig. 3C) reveals three distinct peaks: lattice oxygen (O^{2-}) at 529.52 eV, indicating the stability of the spinel structure, adsorbed oxygen species (O_ads) at 531.25 eV, which contribute to catalytic activity, and physically adsorbed water (H_2O) at 532.57 eV, representing surface-bound species.

3.2 Hydrogen evolution reaction

The electrochemical performance of Nb-doped Co_3O_4 nanosheets on nickel foam was evaluated using a three-electrode system in an alkaline electrolyte. Fig. 4A presents the linear sweep voltammetry results recorded at a scan rate of 5 mV s^{-1}, showing a distinct cathodic current response for the HER across NF, CO/NF, 1NCO/NF, 2NCO/NF, 3NCO/NF, and 4NCO/NF, where nickel foam exhibits the poorest activity. In contrast, Nb-doped Co_3O_4/NF with an optimized Nb content demonstrates significantly enhanced HER performance compared to pristine CO/NF. Among all tested electrodes, the 3NCO/NF electrode unveils the best HER activity, requiring an overpotential of 196 mV *vs.* RHE at 10 mA cm^{-2} and 289 mV *vs.* RHE at 100 mA cm^{-2}. Additionally, 3NCO/NF shows the most favourable potential across all current densities. The electrodes exhibit overpotentials (η) of 267 mV *vs.* RHE, 258 mV *vs.* RHE, 248 mV *vs.* RHE, and 215 mV *vs.* RHE at 10 mA cm^{-2} for CO/NF, 1NCO/NF, 2NCO/NF, and 4NCO/NF, respectively. The significantly lower overpotential of 3NCO/NF highlights the

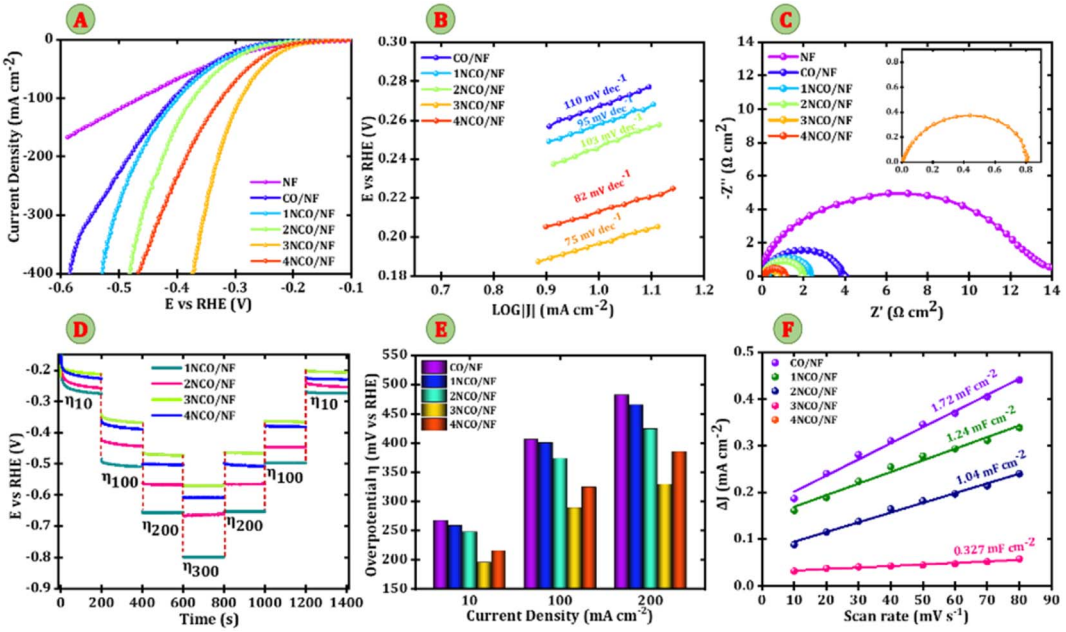

Fig. 4 Electrocatalytic performance for the hydrogen evolution reaction (HER) in 1.0 M KOH. (A) Linear sweep voltammetry (LSV) curves, (B) corresponding Tafel slopes, (C) Nyquist plots from electrochemical impedance spectroscopy (EIS), (D) multi-step chronopotentiometry to evaluate operational stability, (E) overpotential comparison at 10 mA cm^{-2}, and (F) double-layer capacitance (C_{dl}) values of CO/NF and Nb-doped Co_3O_4/NF electrodes (1NCO, 2NCO, 3NCO, and 4NCO), highlighting the effect of Nb doping on HER performance.

effectiveness of 3% Nb doping in enhancing HER activity, making it the most efficient catalyst among the tested compositions. The Tafel plots were derived from polarization curves to analyse the HER kinetics (Fig. 4B). The Tafel slope of 3NCO/NF is 75 mV dec^{-1}, compared to 103 mV dec^{-1} for CO/NF, 95 mV dec^{-1} for 1NCO/NF, 103 mV dec^{-1} for 2NCO/NF, and 82 mV dec^{-1} for 4NCO/NF. The lower Tafel slope observed for the 3NCO/NF electrode indicates enhanced hydrogen evolution reaction (HER) kinetics, signifying a more efficient electron transfer process at the electrode–electrolyte interface. The Tafel slopes for all electrodes fall between the characteristic values of the Heyrovsky (~40 mV dec^{-1}) and Volmer (~120 mV dec^{-1}) steps, suggesting that the HER proceeds *via* the Volmer–Heyrovsky mechanism. This implies that both the initial electrochemical dissociation of water molecules to form adsorbed hydrogen intermediates (Volmer step) and their subsequent electrochemical desorption through interaction with another water molecule (Heyrovsky step) are kinetically significant.[27] Notably, the 3NCO/NF electrode exhibits the lowest Tafel slope within the series, pointing to the Heyrovsky step as the likely rate-determining step. This observation implies more commending kinetics for the electrochemical desorption of adsorbed hydrogen intermediates, thereby enhancing the overall HER activity. To gain deeper insights into the electronic charge transport mechanism, electrochemical impedance spectroscopy (EIS) was performed. The Nyquist plot, shown in Fig. 4C, exhibits a characteristic semicircle that corresponds to the charge transfer resistance (R_{ct}) at the electrode–electrolyte interface, providing a direct measure of the efficiency of electron transfer during the electrochemical reaction. The R_{ct} values extracted from the fitting of the equivalent circuit model for the various electrodes are as follows: 4.04 Ω cm^2 for CO/NF, 2.30 Ω cm^2 for 1NCO/NF, 1.92 Ω cm^2 for 2NCO/NF, 0.80 Ω cm^2 for 3NCO/NF, 1.18 Ω cm^2 for 4NCO/NF, and 18.0 Ω cm^2 for bare NF. Notably, the 3NCO/NF electrode demonstrates the lowest R_{ct}, indicating a marked improvement in charge transport efficiency, which can be attributed to its superior conductivity. This enhancement is likely the result of the optimized hydrogen adsorption energy, which is a consequence of the modified electronic structure of the 3NCO/NF electrode. Furthermore, the synergistic effects of Nb doping and the multichannel electronic transport facilitated by the porous nanostructure of 3NCO/NF lead to a significant reduction in charge-transfer resistance. These structural and electronic optimizations directly contribute to the enhanced hydrogen evolution reaction (HER) kinetics, as they facilitate faster electron transfer and lower overpotentials during water splitting. Fig. 4D presents a multi-step chrono-potentiometry analysis performed at various current densities (10, 100, 200, and 300 mA cm^{-2}) to assess the charge transfer and mass transport efficiency of the electrodes. The 3NCO/NF electrode exhibits stable electronic charge transport across the entire range of current densities, indicating robust performance under high-demand conditions. Moreover, the dimensionally stable 3NCO/NF electrode demonstrates effective mass transport, as evidenced by the step-like potential transitions that occur with changes in current density. These transitions highlight the electrode's ability to maintain efficient electrochemical processes even at high current densities. The overpotentials (η) of the various electrodes are compared in the bar chart shown in Fig. 4E. The 3NCO/NF electrode shows significantly lower overpotentials, with values of 196 mV, 289 mV, and 329 mV *vs.* RHE at current densities of 10, 100, and

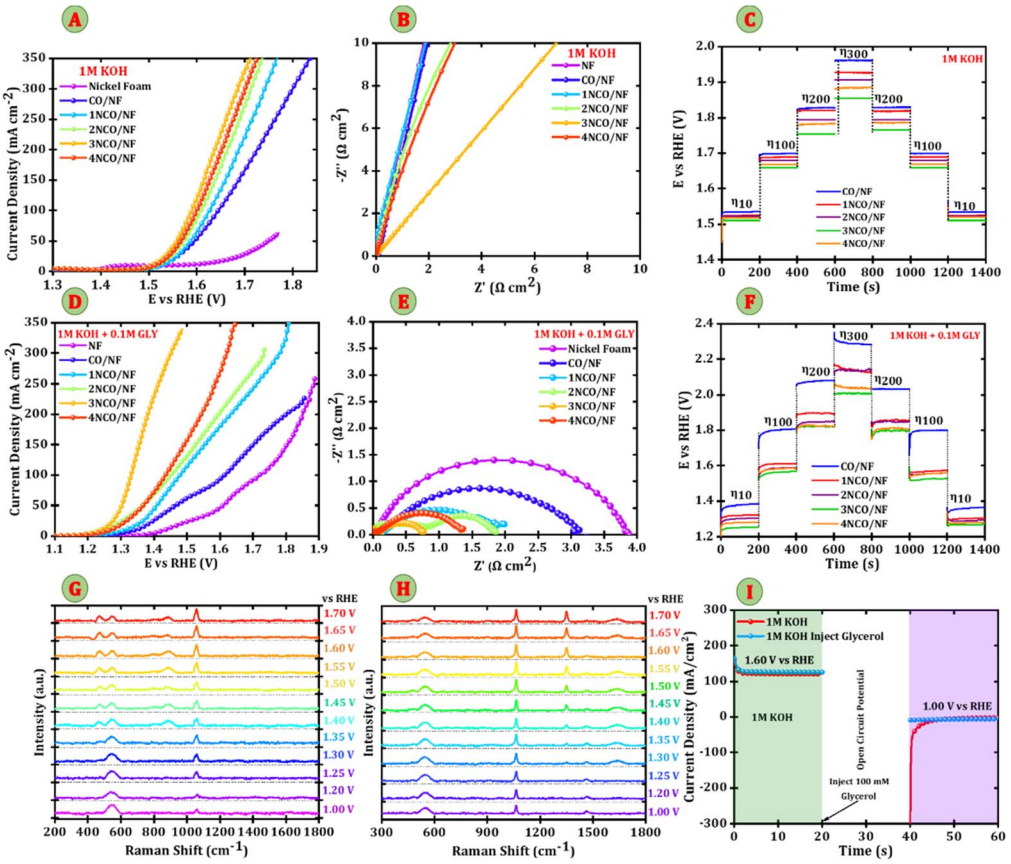

Fig. 5 Oxygen evolution reaction performance: (A) linear sweep voltammetry curve, (B) Nyquist plots, (C) step chronopotentiometry in 1 M KOH. Glycerol oxidation reaction performance: (D) linear sweep voltammetry curve, (E) Nyquist plots, (F) step chronopotentiometry in 1 M KOH + 0.1 M glycerol of CO/NF and 1NCO/NF, 2NCO/NF, 3NCO/NF, and 4NCO/NF. *In situ* Raman spectra of 3NCO/NF at varied potentials in (G) 1 M KOH, and (H) 1 M KOH + 0.1 M glycerol, and (I) chronoamperometric curves of 3NCO/NF in 1 M KOH, and 1 M KOH + 0.1 M glycerol.

200 mA cm^{-2}, respectively. These values outperform both pristine Co_3O_4/NF and other Nb-doped Co_3O_4/NF electrodes, demonstrating superior catalytic efficiency for the hydrogen evolution reaction (HER). This superior performance can be attributed to the enhanced electrochemical activity and optimized structural characteristics of the 3NCO/NF electrode, which facilitate both charge transfer and mass transport during water splitting. To further evaluate the intrinsic catalytic activity and electrochemically active surface area (ECSA) of the electrodes, cyclic voltammetry (CV) curves were recorded at various scan rates within the non-faradaic potential region (Fig. S3(A–E)). These measurements were used to calculate the double-layer capacitance (C_{dl}), which serves as a proxy for the ECSA and provides valuable insight into the surface properties and electrochemical behaviour of the electrodes. The calculated C_{dl} values for the electrodes are as follows: 1.72 mF cm^{-2} for CO/NF, 1.24 mF cm^{-2} for 1NCO/NF, 1.04 mF cm^{-2} for 2NCO/NF, 0.327 mF cm^{-2} for 3NCO/NF, and 1.10 mF cm^{-2} for 4NCO/NF (Fig. 4F). These values indicate that the 3NCO/NF electrode, with its lower C_{dl}, has a more compact electrochemical double layer, suggesting a higher density of electrochemically active sites. Since electrocatalytic performance depends on both the electrochemically active surface area and intrinsic catalytic activity, the turnover frequency (TOF) was calculated to further evaluate the intrinsic activity of the synthesized electrodes. The obtained TOF values are 0.48 s^{-1} for CO/NF, 0.68 s^{-1} for 1NCO/NF, 0.74 s^{-1} for 2NCO/NF, 2.54 s^{-1} for 3NCO/NF, and 0.79 s^{-1} for 4NCO/NF. Among them, the 3NCO/NF electrode demonstrates the highest TOF of 2.54 s^{-1} at a current density of 10 mA cm^{-2}, clearly outperforming the other samples and previously reported catalysts (Fig. S3(F)). Furthermore, normalization of the ECSA for each electrode (Fig. S3(G)) confirms the enhanced electrochemical surface area of the 3NCO/NF electrode. The 3NCO/NF electrode exhibits superior hydrogen evolution reaction (HER) performance, demonstrated by its lowest Tafel slope and overpotential compared to the other electrodes. In terms of stability, the 3NCO/NF electrode retains excellent HER catalytic stability, as shown by chronopotentiometry measurements at 200 mA cm^{-2}, where only a minimal change in current density is observed over a 14-hour period (Fig. S3(H)), indicating negligible degradation in catalytic performance.

3.3 Oxygen evolution and glycerol oxidation

Following the investigation of the hydrogen evolution reaction (HER) activity, the focus was shifted to the evaluation of the oxygen evolution reaction (OER), which is critical for enabling

efficient overall water splitting. A significant positive shift in the OER onset potential was observed, indicating an enhancement in the intrinsic catalytic activity of the electrodes. This observation underscores the importance of a comprehensive analysis of OER kinetics in alkaline electrolytes to fully understand the electrochemical performance of the catalyst. Thus, the OER characteristics of the 3NCO/NF electrode were systematically studied and compared against those of bare NF, 1NCO/NF, 2NCO/NF, and 4NCO/NF electrodes. The electrocatalytic activity for the OER was evaluated in both 1.0 M KOH and a mixed electrolyte of 1.0 M KOH + 0.1 M glycerol. Glycerol, a trihydric alcohol, is a key platform molecule for electrooxidation, facilitating its conversion into value-added chemicals during electrochemical reactions. Fig. 5A presents the linear sweep voltammetry (LSV) curves of bare NF, 1NCO/NF, 2NCO/NF, 3NCO/NF, and 4NCO/NF electrodes at a scan rate of 5 mV s^{-1} in 1.0 M KOH electrolyte. Each electrode exhibits two distinct anodic peaks within the potential range of 1.20 to 1.55 V *vs.* RHE, as shown in Fig. S4(A), corresponding to the oxidation of Co sites and the OER response. This behaviour suggests a two-step oxidative reconstruction process, where Co^{2+} is first oxidized to Co^{3+}, followed by a further oxidation to Co^{4+}, ultimately resulting in the formation of (hydro)oxide species.[28] These higher-valence Co sites are well-established as the primary active centres for the oxygen evolution reaction (OER). Notably, the incorporation of Nb sites further enhances OER performance by promoting the efficient stabilization and optimization of reaction intermediates, thereby accelerating the overall catalytic process.[29]

Nb modulation of oxygen binding strength plays a crucial role in striking a balance between stability and desorption, facilitating the efficient formation of OH* and O* intermediates. This precisely tuned interaction enhances the OER kinetics, leading to improved catalytic activity of the electrode. Among the electrodes tested, the 3NCO/NF electrode exhibits superior OER performance, achieving current densities of 10 mA cm^{-2} and 100 mA cm^{-2} with low overpotentials of 1.50 V *vs.* RHE and 1.58 V *vs.* RHE, respectively. In comparison, the control electrodes—NF (1.50 V *vs.* RHE), CO/NF (1.53 V *vs.* RHE, 1.64 V *vs.* RHE), 1NCO/NF (1.52 V *vs.* RHE, 1.62 V *vs.* RHE), 2NCO/NF (1.51 V *vs.* RHE, 1.60 V *vs.* RHE), and 4NCO/NF (1.51 V *vs.* RHE, 1.59 V *vs.* RHE)—demonstrate relatively higher overpotentials, thereby highlighting the exceptional OER performance of the 3NCO/NF electrode. At an overpotential of 1.71 V *vs.* RHE, the 3NCO/NF electrode exhibits outstanding oxygen evolution reaction (OER) performance, delivering a high current density of 350 mA cm^{-2}. As shown in Fig. 5B, the Nyquist plots highlight both the series resistance (R_s) and the charge transfer resistance (R_{ct}) of the electrodes. Notably, the 3NCO/NF electrode demonstrates the lowest R_{ct} value of 0.6 Ω cm^2, suggesting significantly improved electrical conductivity and efficient charge transfer at the electrode–electrolyte interface. This reduction in R_{ct} is a key indicator of enhanced electrochemical kinetics, which is crucial for optimizing OER performance. The observed enhancement in conductivity and charge transfer is attributed to the Nb doping, which promotes better electron transport through the strong covalent bonding between Nb and Co, as well as the improved contact between Co–O bonds. This modification not only facilitates efficient electron transfer but also stabilizes the active sites, which further contributes to the overall catalytic efficiency of the 3NCO/NF electrode.[30] To compare, the bare NF shows a higher R_{ct} of 16 Ω cm^2, and other electrodes, such as CO/NF, 1NCO/NF, 2NCO/NF, and 4NCO/NF, exhibit R_{ct} values of 1.17 Ω cm^2, 1.01 Ω cm^2, 0.81 Ω cm^2, and 0.77 Ω cm^2, respectively. Fig. 5C shows the multi-step chronopotentiometry curves at various current densities ranging from 10 to 300 mA cm^{-2} to comprehend the efficacy of charge transfer and mass transport. The potential values exhibit stability across a range of current values, suggesting stable electronic charge-transport of 3NCO/NF electrodes. The 3NCO/NF electrode demonstrates excellent OER performance with its low overpotential, minimal R_{ct}, and R_s, alongside outstanding stability for reliable, long-term operation. Also, the stability of the 3NCO/NF electrode was confirmed through chronopotentiometry analysis at 200 mA cm^{-2}, showing no significant change in current density over 12 hours, highlighting its high OER catalytic stability (Fig. S4(B)).

Fig. 5D presents the linear sweep voltammetry (LSV) curves for glycerol electrooxidation in an alkaline medium (1 M KOH + 0.1 M glycerol). In contrast to the oxygen evolution reaction (OER), glycerol oxidation reaction (GOR) occurs at significantly lower potentials, demonstrating both thermodynamic and kinetic advantages. Notably, the enhanced anodic response, particularly in the Nb-doped electrodes, indicates that Nb incorporation facilitates the oxidation of Co active sites by improving chemisorption and enhancing electronic interactions with glycerol molecules. The addition of 0.1 M glycerol leads to a marked increase in anodic current above 1.20 V *vs.* RHE, which is considerably lower than the typical OER onset potential of approximately 1.55 V *vs.* RHE. This suggests more favorable glycerol oxidation kinetics. The anodic activity observed between 1.20 V and 1.55 V *vs.* RHE is primarily attributed to glycerol oxidation, aligning with the characteristic reactivity of glycerol as a polyol, which can undergo oxidation at relatively low potentials due to its multiple hydroxyl groups. The 3NCO/NF electrode demonstrates superior GOR performance, requiring an ultralow potential of 1.19 V *vs.* RHE and 1.30 V *vs.* RHE to achieve current densities of 10 mA cm^{-2} and 100 mA cm^{-2}, respectively. In comparison, the control electrodes—CO/NF (1.34 V *vs.* RHE, 1.61 V *vs.* RHE), 1NCO/NF (1.31 V *vs.* RHE, 1.47 V *vs.* RHE), 2NCO/NF (1.24 V *vs.* RHE, 1.45 V *vs.* RHE), 4NCO/NF (1.26 V *vs.* RHE, 1.43 V *vs.* RHE), and Ni foam (1.43 V *vs.* RHE, 1.71 V *vs.* RHE)—require higher potentials, further underscoring the superior GOR activity of the 3NCO/NF electrode. This enhanced performance is likely attributed to the synergistic effects of Nb doping, which not only improves charge transfer efficiency but also optimizes the adsorption and activation of glycerol molecules on the catalyst surface, thus promoting faster and more efficient glycerol oxidation. The charge-transfer resistances, represented by the arc diameters, were measured to be 3.87, 3.08, 2.00, 1.85, 0.74, and 1.35 Ω cm^2 for bare NF, CO/NF, 1NCO/NF, 2NCO/NF, 3NCO/NF, and 4NCO/NF electrodes, respectively. These results indicate that the 3NCO/NF electrode exhibits the highest catalytic efficiency for

glycerol oxidation reaction (GOR). The GOR stability of the 1NCO/NF, 2NCO/NF, 3NCO/NF, and 4NCO/NF electrodes was assessed using chronopotentiometry at various current densities (10, 100, 200, and 300 mA cm^{-2}, as shown in Fig. 5F). The observed initial decline in potential (V), followed by the establishment of stable plateaus, suggests that these electrodes maintain good catalytic stability. This initial drop in potential is more pronounced at higher current densities, likely due to the faster consumption of glycerol and hydroxide ions at the electrode surface. Based on these findings, the catalyst demonstrates excellent conductivity and efficient mass transport. The potential stabilization and sustained catalytic activity at high current densities underscore the electrode's robust operational durability and superior intrinsic electrocatalytic efficiency.

Fig. S5 presents a bar chart illustrating potential at 10 mA cm^{-2} for the CO/NF, 1NCO/NF, 2NCO/NF, 3NCO/NF, and 4NCO/NF electrodes in both 1 M KOH and 1 M KOH + 0.1 M glycerol electrolytes. The chart highlights that the 3NCO/NF electrode exhibits the lowest overpotential at 10 mA cm^{-2} in both electrolytes, outperforming the CO/NF, 1NCO/NF, 2NCO/NF, and 4NCO/NF electrodes. This suggests its superior electrocatalytic performance, requiring less energy to achieve the same current density and thereby demonstrating enhanced efficiency for both the oxygen evolution reaction (OER) and glycerol oxidation reaction (GOR). Furthermore, the 3NCO/NF electrode is capable of catalyzing the electrooxidation of various alcohols, including ethanol (EtOH), methanol (MtOH), glycerol, urea, and ethylene glycol (EG), as shown in Fig. S6(A). Despite exhibiting less pronounced anodic responses compared to typical GOR profiles, the 3NCO/NF electrode demonstrates excellent stability and activity for glycerol oxidation, making it a promising candidate for efficient GOR applications. Fig. S5(B) presents a bar chart comparing the overpotential at different current densities for the 3NCO/NF electrode across various electrolytes: ethanol (EtOH), methanol (MtOH), glycerol (Gly), urea, and ethylene glycol (EG). In Fig. S6(B), at 10 mA cm^{-2}, glycerol shows the lowest overpotential (0.20 V *vs.* RHE), followed by ethylene glycol (0.46 V *vs.* RHE), urea (0.57 V *vs.* RHE), ethanol (0.94 V *vs.* RHE), and methanol (0.60 V *vs.* RHE). At 100 mA cm^{-2}, glycerol again demonstrates the lowest overpotential (0.38 V *vs.* RHE), while ethylene glycol (0.48 V *vs.* RHE), urea (0.57 V *vs.* RHE), methanol (0.94 V *vs.* RHE), and ethanol (0.73 V *vs.* RHE) show progressively higher values. This analysis underscores the exceptional catalytic activity of the 3NCO/NF electrode, particularly for the GOR. The low overpotential observed in glycerol confirms that the 3NCO/NF electrode efficiently facilitates the GOR, requiring less energy to reach the desired current density. This enhanced efficiency is attributed to the electrode's optimal mass transport properties and outstanding conductivity, which significantly improve its performance in glycerol oxidation. A comprehensive literature review (Table S1) was conducted to benchmark the performance of the synthesized Nb-Co_3O_4/NF electrocatalyst against various state-of-the-art electrocatalysts in a three-electrode electrochemical setup. This comparative analysis involved evaluating a key performance metric that is overpotential in a KOH + glycerol environment. The findings underscore the competitive edge of Nb-Co_3O_4/NF in glycerol electrooxidation, particularly in terms of formate production efficiency.

To elucidate the potential-dependent surface chemistry of the Nb-Co_3O_4 catalyst under electrochemical conditions, *in situ* Raman spectroscopy was conducted in both alkaline (1 M KOH) and glycerol-containing (1 M KOH + 0.1 M glycerol) electrolytes over a potential range of 1.0–1.7 V *vs.* RHE. In pure KOH (Fig. 5G), characteristic Raman bands at ~515 cm^{-1} were consistently observed across all potentials, corresponding to the F_{2g} vibrational modes of the Co_3O_4 spinel structure. Notably, the ~470 cm^{-1} E_g mode, associated with Co^{3+}–O vibrations in octahedral sites, exhibited a clear increase in intensity beginning at 1.35 V *vs.* RHE, suggesting enhanced oxidation of Co^{2+} to Co^{3+} at this potential. This spectral evolution is consistent with the gradual transformation of surface Co^{2+} species into higher-valent Co^{3+}, reflecting the early stages of surface activation. Concurrently, a broad feature at ~810 cm^{-1} began to emerge and intensified with increasing potential, indicative of the formation of cobalt oxyhydroxide (CoOOH), the known catalytically active phase for the OER. In stark contrast, the Raman spectra collected in 1 M KOH + 0.1 M glycerol (Fig. 5H) exhibited a suppression of oxyhydroxide-related features and the emergence of distinct bands associated with glycerol-derived oxidation intermediates. While the spinel Co_3O_4 backbone band at ~515 cm^{-1} remained detectable, the CoOOH-associated band at ~810 cm^{-1} was significantly attenuated across the entire potential range, suggesting that glycerol electrooxidation predominates over the OER and prevents substantial surface reconstruction into cobalt oxyhydroxide phases. Starting at 1.20 V *vs.* RHE, a peak at ~1045 cm^{-1} emerged, attributed to C–OH bending or C–C stretching vibrations of adsorbed glycerol species. Notably, a band at ~1350 cm^{-1} appeared at 1.30 V *vs.* RHE, signalling the formation of carboxylate (COO^-) groups, likely formate, through C–C bond cleavage. The progressive increase in intensity of this peak with rising potential provides strong evidence for ongoing oxidative transformation of glycerol into highly valuable formate. Furthermore, the appearance of a distinct band at ~1629 cm^{-1} at higher potentials, corresponding to asymmetric stretching of C=O or COO^- groups, reinforces the formation of oxygenated intermediates such as glyceraldehyde and formate. This behavior indicates that Nb-Co_3O_4 resists significant surface reconstruction and favors surface-bound *OH-mediated oxidation instead. These findings strongly suggest that *niobium incorporation into the Co_3O_4 spinel framework enhances the density of surface hydroxyl (OH) species and stabilizes glycerol-derived intermediates, thereby promoting selective and energy-efficient glycerol oxidation while suppressing competing oxygen evolution reaction (OER) activity. To further substantiate this mechanistic insight, a multi-potential step experiment (Fig. 5I) was conducted to differentiate between direct and indirect oxidation pathways. Surface CoOOH was first generated at 1.60 V *vs.* RHE, followed by an open-circuit potential (OCP) hold during glycerol injection, and then a cathodic bias at 1.00 V was applied. The complete absence of a reduction current during this final step confirms that no spontaneous chemical reaction occurs between glycerol and the electrogenerated CoOOH, effectively

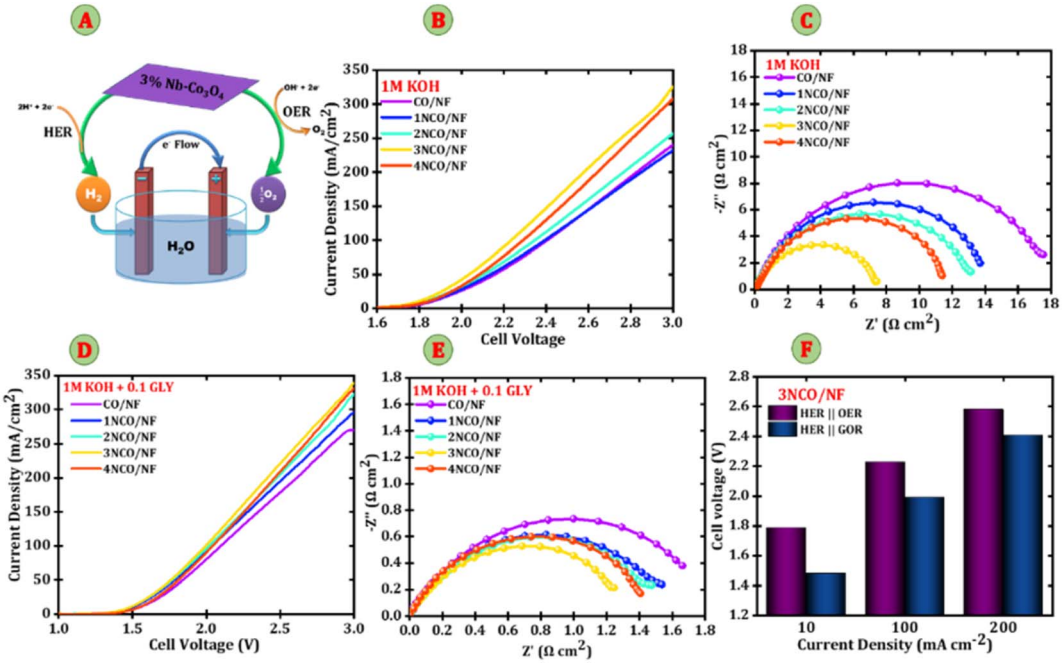

Fig. 6 Overall electrolysis performance of coupling the anodic OER and GOR with the cathodic HER. (A) Schematic illustration of the overall electrolysis configuration, (B) LSV polarization curves, (C) Nyquist plots in 1 M KOH and (D) LSV polarization curves. (E) Nyquist plots in 1 M KOH + 0.1 M glycerol, (F) cell voltage comparision of 3NCO/NF at various current density for both OER and GOR.

ruling out an indirect oxidation mechanism. These combined spectroscopic and electrochemical findings unambiguously establish that Nb-Co_3O_4 catalyzes glycerol electrooxidation *via* a direct surface-mediated process involving Co^{2+}/Co^{3+} redox transitions and *OH-assisted proton-coupled electron transfer, without requiring participation from bulk oxyhydroxide intermediates.

3.4 Bi-functional electrolysis

After confirming the outstanding HER, OER, and GOR performances of Nb-doped Co_3O_4 electrodes, a full electrolyzer cell was constructed using Nb-Co_3O_4 as both the anode and cathode for overall water splitting. Additionally, NCO/NF electrodes were configured in a two-electrode system, serving as the cathode and anode, to investigate overall water splitting and glycerol electrolysis. During electrolysis, the simultaneous generation of O_2 and formate at the anode, along with H_2 evolution at the cathode, highlights the efficiency of the electrocatalytic process. This synergistic reaction enhances oxygen evolution and glycerol oxidation while facilitating sustainable hydrogen production.[31,32] The electrochemical experiments were conducted in a 1 M KOH solution, with 0.1 M glycerol introduced to evaluate its impact on glycerol electrolysis. The LSV curves in Fig. 6B (measured in 1 M KOH) show that the driving potentials required to reach a current density of 10 mA cm^{-2} are 1.86 V, 1.84 V, 1.82 V, 1.79 V, and 1.83 V for the CO/NF, 1NCO/NF, 2NCO/NF, 3NCO/NF, and 4NCO/NF electrodes, respectively. Fig. 6C displays the Nyquist plot, which illustrates the kinetics of water electrolysis in 1 M KOH. The plot reveals charge transfer resistance (R_{ct}) values of 17.62, 13.66, 13.07, 7.36, and 11.33 Ω cm^2 for the CO/NF, 1NCO/NF, 2NCO/NF, 3NCO/NF, and 4NCO/NF electrodes, respectively. Particularly, the 3NCO/NF electrode exhibits the lowest R_{ct} value (7.36 Ω cm^2), indicating a more rapid charge transfer process between the electrode and the electrolyte interface. This enhanced kinetics can be attributed to the introduction of Nb, which optimizes the electronic structure and improves the intrinsic conductivity of Co_3O_4, thereby accelerating reaction dynamics and boosting overall catalytic performance. However, the introduction of 0.1 M glycerol into the 1 M KOH electrolyte suggests that glycerol may influence the electrochemical environment by modifying surface adsorption properties or altering reaction kinetics, thereby potentially impeding overall catalytic efficiency. Fig. 6D presents the LSV curves, showing that the incorporation of 0.1 M glycerol into 1 M KOH results in driving potentials of 1.54 V, 1.49 V, 1.47 V, 1.46 V, and 1.53 V at a current density of 10 mA cm^{-2} for the CO/NF, 1NCO/NF, 2NCO/NF, 3NCO/NF, and 4NCO/NF electrodes, respectively, with the 3NCO/NF electrode exhibiting the lowest value among all. It can be inferred from Fig. 6A and D that, at a higher current density of 100 mA cm^{-2}, the anodic potentials for the OER and GOR are recorded at 2.23 V and 1.99 V, respectively, demonstrating that the GOR process requires 240 mV less potential than the OER. This reduction highlights that the presence of glycerol significantly decreases the energy input required for electrolysis. Furthermore, the Nyquist plot in Fig. 6E shows that the R_{ct} values for these electrodes are 1.66 Ω cm^2, 1.55 Ω cm^2, 1.47 Ω cm^2, 1.25 Ω cm^2, and 1.40 Ω cm^2 for the CO/NF, 1NCO/NF, 2NCO/NF, 3NCO/NF, and 4NCO/NF electrodes, respectively, confirming improved charge transfer kinetics in the glycerol-assisted

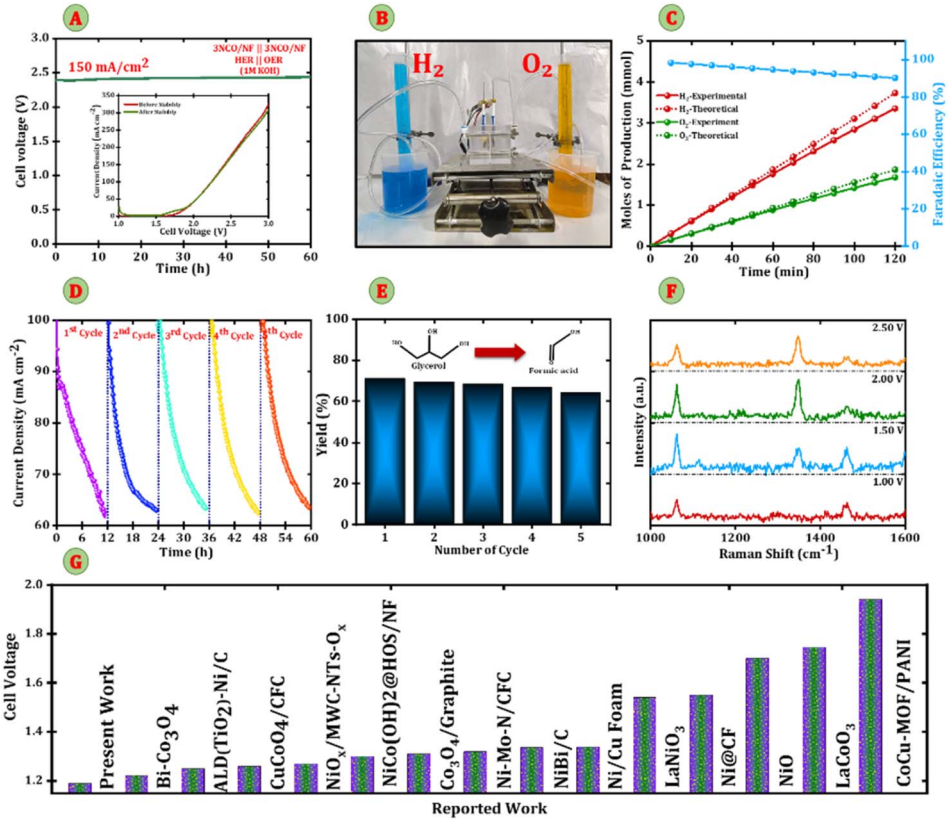

Fig. 7 (A) Long-term stability by chronopotentiometry of 3NCO/NF in 1 M KOH, (B) photograph of the H-cell electrolyzer setup used for the experiments. (C) Faradaic efficiency of 3NCO/NF in 1 M KOH, (D) five *J*–*t* cycles of the electrolyzer at 2.0 V voltage in 1 M KOH + 0.1 M glycerol for glycerol electrolysis, (E) yield calculation of number of cycles, (F) Raman spectra recorded at different applied potentials.

environment. Notably, the 3NCO/NF electrode delivers a current density of 100 mA cm^{-2} with impressive water electrolysis and glycerol electrolysis performance at cell voltages of 2.23 V in 1 M KOH and 1.99 V in 1 M KOH with 0.1 M glycerol, respectively, further emphasizing the critical role of Nb doping in enhancing catalytic activity and energy efficiency.

Furthermore, to evaluate the long-term stability of the 3NCO/NF electrode, chronopotentiometry was conducted at a constant current density of 150 mA cm^{-2}, as depicted in Fig. 7A. The results demonstrate that the electrode maintains a steady potential of 2.38 V for approximately 60 hours in 1 M KOH, indicating excellent stability during overall water electrolysis. The inset plot in Fig. 7A shows the before and after LSV curves to highlight the minimal degradation in electrochemical performance. Also, Fig. S7 presents the FESEM images and corresponding EDX elemental mapping, confirming the preserved morphology and uniform elemental distribution of the catalyst after the stability test. This prolonged stability, coupled with its superior electrochemical performance, underscores the potential of the 3NCO/NF electrode as a highly promising candidate for industrial applications in water electrolysis. Further investigation into the electrolysis process was carried out at a constant current density of 100 mA cm^{-2} using chronoamperometry, during which the evolution of hydrogen (H_2) and oxygen (O_2) gases was meticulously monitored. Fig. 7B shows a digital photograph of the experimental setup used for faradaic efficiency measurements, highlighting the gas collection apparatus employed. The results, shown in Fig. 7C, indicate that the volumes of H_2 and O_2 produced are in close agreement with theoretical predictions, with the molar ratio of H_2 to O_2 remaining consistently around 2 : 1, as expected for water splitting reactions. In addition, Fig. S8 presents a series of digital photographs captured at 30, 60, 90, and 120 minutes, illustrating the accumulated volumes of H_2 and O_2 gases over time. The measured gas volumes are as follows: at 30 minutes, approximately 20 mL of H_2 and 10 mL of O_2; at 60 minutes, 39 mL of H_2 and 19 mL of O_2; at 90 minutes, 57 mL of H_2 and 28 mL of O_2; and at 120 minutes, 75 mL of H_2 and 37 mL of O_2. These results demonstrate the expected 2 : 1 stoichiometric ratio of hydrogen to oxygen, consistent with water electrolysis. The images further validate the sustained generation and collection of gases in this ideal molar ratio throughout the entire experimental period. The faradaic efficiency (FE) was initially measured at 99%, but it gradually decreased to approximately 90% over the course of the experiment. The hydrogen production rate was calculated to be 1.56 mmol h^{-1}, highlighting the high electrocatalytic activity and sustained performance of the 3NCO/NF electrode during prolonged electrolysis.[33] The 3NCO/NF electrode exhibits superior electrochemical performance compared to commercially available

alternatives. Fig. S9 demonstrates the outstanding catalytic performance of 3NCO/NF in the GOR during chronopotentiometry measurements at a constant current density of 50 mA cm^{-2} with a potential of 1.99 V; the immediate addition of 10 μL of glycerol to the 1 M KOH electrolyte results in a sharp 230 mV reduction in the reaction potential, dropping to 1.76 V. This substantial decrease underscores the rapid and efficient response of the 3NCO/NF catalyst in facilitating the GOR. Also, to evaluate the long-term stability of the electrolyzer during glycerol electrooxidation, a constant potential of 2.0 V was applied for 12 hours. The electrochemical behavior was monitored over five consecutive *J–t* cycles, as shown in Fig. 7D. Throughout the experiment, a slight decline in current density (*J*) was observed, suggesting a gradual reduction in efficiency as the reaction progressed through glycerol oxidation to formic acid production. After 12 hours of electrolysis, refreshing the electrolyte successfully restored the potential, demonstrating the reversibility and lasting stability of the 3NCO/NF electrode during extended operation. Fig. S10 shows FESEM images and EDX mapping after the GOR stability test, illustrating retained morphology, consistent elemental distribution, and incorporation of potassium from the alkaline electrolyte. XRD patterns recorded in 1 M KOH and 1 M KOH + 0.1 M glycerol electrolytes show no significant changes in the crystal structure, confirming the structural stability of the catalyst under both conditions, Fig. S11. This led to the coproduction of hydrogen (H_2) and formate ions, with yields that highlight the strong industrial potential of the 3NCO/NF‖3NCO/NF electrolyzer. To further assess formate production, high-performance liquid chromatography (HPLC) was employed to quantify the formate ion concentration after each 12-hour electrolysis cycle. Distinct peaks of formate were observed in the chromatograms, confirming the formation and accumulation of formic acid throughout the electrooxidation process (Fig. S12). The amount of formic acid produced was determined using a standard calibration curve, constructed by plotting known concentrations of formic acid against their corresponding HPLC peak areas. Integration of the formic acid peak showed consistent signals across all five cycles, with a gradual decrease in peak intensity, suggesting slight catalyst deactivation while still maintaining significant production rates. The calculated yields of formate after each cycle are summarized in the bar diagram shown in Fig. 7E. The corresponding ^1H NMR analysis of the product (Fig. S13) exhibited peaks consistent with the standard formate, further confirming the formation of formate. To investigate the electrochemical oxidation of glycerol and confirm the formation of formate (FA), *ex situ* Raman spectroscopy was performed on the electrode surface after 6 hours of glycerol electrolysis at applied potentials of 1.0, 1.5 V, 2.0 V, and 2.5 V. As shown in Fig. 7F, distinct Raman bands were observed in the regions of 1000–1100 cm^{-1} and 1400–1500 cm^{-1}, which are attributed to characteristic vibrational modes of formate species. The peak around 1050 cm^{-1} corresponds to the symmetric C–O stretching vibration, while the prominent signals at 1348 cm^{-1} are associated with the asymmetric stretching of the formate, consistent with reported Raman signatures of formic acid or its deprotonated form.[34] The intensity of these peaks increases with the applied potential, reaching a maximum at 2.0 V, which suggests that this potential favours the accumulation of formate on the catalyst surface. However, a subsequent decrease in intensity at 2.5 V may be attributed to the dominance of the oxygen evolution reaction (OER), which competes with the glycerol oxidation pathway and can degrade the selective formation of formic acid. These *ex situ* Raman observations strongly support the presence of formate ion as a major product in glycerol oxidation, and reflect the influence of applied potential on product distribution and surface reaction dynamics.[35] Raman spectroscopy detects formate ions because it probes molecular vibrations of species in their ionic form in solution, while HPLC identifies formic acid due to acidified mobile phases suppressing ionization, causing formate to exist predominantly as undissociated formic acid during analysis.[36] A renewable solar-energy-driven electrolyzer (SN 5) was developed for efficient hydrogen production *via* alkaline water electrolysis. The system operates stably at 1.79 V using a solar cell, and glycerol oxidation lowers energy input while enabling the production of hydrogen and oxygen. Notably, the electrolyzer maintained a consistent operating voltage over a continuous 2-hour test, as shown in Fig. S14, confirming its excellent durability under solar-driven conditions. This approach offers a sustainable and decentralized solution for clean energy generation.[37]

To further explore the industrial-scale potential of the 3NCO/NF catalyst, its bifunctional water-splitting activity was evaluated by varying the KOH concentration (1, 2, 4, and 6 M) at room temperature. Fig. S15(A) shows that in 1 M KOH, the 3NCO/NF‖3NCO/NF cell requires 1.79 V to achieve a current density of 10 mA cm^{-2}, while in 6 M KOH, the required potential is 1.73 V. The Nyquist plot in Fig. S15(B) indicates a decrease in charge-transfer resistance as the KOH concentration increases, particularly in 6 M KOH. This decrease is associated with a faster charge transfer rate at the electrode–electrolyte interface. The enhanced ionic conductivity in 6 M KOH leads to lower charge-transfer resistance, higher current density, and a lower overall cell voltage, resulting in a more efficient and rapid water-splitting process. Fig. S15(C) illustrates the LSV of the 3NCO/NF electrode at different glycerol concentrations. The anodic response increases with glycerol concentration up to 0.1 M, demonstrating a more effective GOR at higher concentrations. However, the response diminishes slightly below 1.42 V, indicating that the optimal electrolyte condition for the GOR is 1 M KOH with 0.1 M glycerol.

4. Conclusions

In conclusion, a 3% niobium-doped Co_3O_4 framework (3NCO/NF) was successfully grown on Ni foam *via* a one-step hydrothermal process, yielding binder-free and additive-free electrode architecture. Structural and spectroscopic analyses (XRD, Raman, XPS) confirmed Nb incorporation into the Co_3O_4 lattice, inducing lattice distortion and electronic modulation that enhanced active site density and charge transport. *In situ* Raman studies revealed that the 3NCO/NF electrode maintained structural integrity during glycerol electro-oxidation

while promoting the formation of formate intermediates. Electrochemical evaluations demonstrated that 3NCO/NF exhibited the best overall performance among all samples, requiring only 196 mV *vs.* RHE for the HER, 1.50 V *vs.* RHE for the OER, and 1.19 V *vs.* RHE for the GOR at 10 mA cm^{-2}, alongside outstanding durability. The electrode sustained efficient operation even under industrially relevant conditions, achieving 1.73 V at 10 mA cm^{-2} in 6 M KOH. Moreover, solar-driven water-splitting tests confirmed its practical applicability for decentralized hydrogen generation. In addition, the 3NCO/NF electrode exhibited remarkable electrochemical stability with negligible performance degradation over extended operation. The multifunctional capability of Nb-Co_3O_4 to co-produce hydrogen and value-added formate establishes a promising pathway for sustainable energy conversion and glycerol valorization. Collectively, these results highlight the potential of Nb-doped Co_3O_4 as a robust and scalable catalyst platform for next-generation renewable energy systems.

Conflicts of interest

There are no conflicts to declare.

Data availability

The data that support the findings of this study are available from the corresponding author upon reasonable request.

Supplementary information (SI): supplementary datasets, raw data, or experimental details related to this study. See DOI: https://doi.org/10.1039/d5ta08434b.

Acknowledgements

The authors gratefully acknowledge the financial support to this research by Charotar University of Science and Technology. S. Rathod, and S. Kapatel are grateful for the "Promotion of University Research in Scientific Excellence (PURSE)" grant by the Department of Science and Technology (DST), Government of India (GoI) (Grant ID: (SR/PURSE/2023/162)).

References

1 M. M. Hossain Bhuiyan and Z. Siddique, Hydrogen as an alternative fuel: a comprehensive review of challenges and opportunities in production, storage, and transportation, *Int. J. Hydrogen Energy*, 2025, **102**, 1026–1044, DOI: 10.1016/j.ijhydene.2025.01.033.

2 J. Ni, *et al.*, Development of noble metal-free electrocatalysts towards acidic water oxidation: From fundamental understanding to state-of-the-art catalysts, *eScience*, 2024, 100295, DOI: 10.1016/j.esci.2024.100295.

3 A. Raveendran, M. Chandran and R. Dhanusuraman, A comprehensive review on the electrochemical parameters and recent material development of electrochemical water splitting electrocatalysts, *RSC Adv.*, 2023, 3843–3876, DOI: 10.1039/d2ra07642j.

4 E. A. Moges, *et al.*, Materials of Value-Added Electrolysis for Green Hydrogen Production, *ACS Mater. Lett.*, 2024, 4932–4954, DOI: 10.1021/acsmaterialslett.4c01173.

5 H. Chen, *et al.*, Highly efficient C@Ni-Pd bifunctional electrocatalyst for energy-saving hydrogen evolution and value-added chemicals co-production from ethanol aqueous solution, *Chem. Eng. J.*, 2023, **474**, 145639, DOI: 10.1016/j.cej.2023.145639.

6 X. Zhang, *et al.*, Enhanced hydrogen production enabled by pulsed potential coupled sulfite electrooxidation water electrolysis system, *Renewable Energy*, 2024, **227**, 120464, DOI: 10.1016/j.renene.2024.120464.

7 A. M. Verma, L. Laverdure, M. M. Melander and K. Honkala, Mechanistic Origins of the pH Dependency in Au-Catalyzed Glycerol Electro-oxidation: Insight from First-Principles Calculations, *ACS Catal.*, 2022, **12**(1), 662–675, DOI: 10.1021/acscatal.1c03788.

8 G. Wu, *et al.*, Anodic glycerol oxidation to formate facilitating cathodic hydrogen evolution with earth-abundant metal oxide catalysts, *Chem. Eng. J.*, 2023, **468**, 143640, DOI: 10.1016/j.cej.2023.143640.

9 A. Rabe, *et al.*, The Roles of Composition and Mesostructure of Cobalt-Based Spinel Catalysts in Oxygen Evolution Reactions, *Chem.–Eur. J.*, 2021, **27**(68), 17038–17048, DOI: 10.1002/chem.202102400.

10 A. K. Beheshti, M. Rezaei, S. M. Alavi, E. Akbari and M. Varbar, Enhanced performance and recyclability of cobalt nanoparticles mesoporous Catalyst supported on mechanochemically prepared CoFe2O4–Co3O4 for sodium borohydride hydrolysis, *Int. J. Hydrogen Energy*, 2024, **93**, 1156–1165, DOI: 10.1016/j.ijhydene.2024.11.019.

11 S. Gupta, R. Fernandes, R. Patel, M. Spreitzer and N. Patel, A review of cobalt-based catalysts for sustainable energy and environmental applications, *Appl. Catal., A*, 2023, **661**, 119254, DOI: 10.1016/j.apcata.2023.119254.

12 C. Zhao, *et al.*, Insights into the electronic origin of enhancing the catalytic activity of Co_3O_4 for oxygen evolution by single atom ruthenium, *Nano Today*, 2020, **34**, 100955, DOI: 10.1016/j.nantod.2020.100955.

13 M. A. Qadeer, *et al.*, A review on fundamentals for designing hydrogen evolution electrocatalyst, *J. Power Sources*, 2024, **613**, 234856, DOI: 10.1016/j.jpowsour.2024.234856.

14 Z. Hu, *et al.*, Advances in dual-site mechanisms for designing high-performance oxygen evolution electrocatalysts, *eScience*, 2025, 100403, DOI: 10.1016/j.esci.2025.100403.

15 V. M. Jiménez-Arévalo, *et al.*, Recent advances in high-entropy alloys for electrocatalysis: From rational design to functional performance, *Mater. Des.*, 2025, **258**, 114633, DOI: 10.1016/j.matdes.2025.114633.

16 W. Xu, P. A. Russo, T. Schultz, N. Koch and N. Pinna, Niobium-Doped Titanium Dioxide with High Dopant Contents for Enhanced Lithium-Ion Storage, *ChemElectroChem*, 2020, **7**(19), 4016–4023, DOI: 10.1002/celc.202001040.

17 R. Y. Chen, *et al.*, A promising Nb-doped La0.5Sr0.5Co0.8Cu0.2O3–δ cathode materials for intermediate temperature solid oxide fuel cells, *J. Alloys*

Compd., 2022, **924**, 166526, DOI: 10.1016/j.jallcom.2022.166526.

18 Y. Wang, *et al.*, Efficient Electrocatalytic Oxidation of Glycerol via Promoted OH* Generation over Single-Atom-Bismuth-Doped Spinel Co3O4, *ACS Catal.*, 2022, **12**(19), 12432–12443, DOI: 10.1021/acscatal.2c03162.

19 Y. Zhu, *et al.*, Iridium single atoms incorporated in Co3O4 efficiently catalyze the oxygen evolution in acidic conditions, *Nat. Commun.*, 2022, **13**, 7754, DOI: 10.1038/s41467-022-35426-8.

20 L. Gao, *et al.*, Embedding Ru single atom catalysts on Co3O4 for efficient hydrazine oxidation and direct hydrazine fuel cells, *Appl. Catal., B*, 2024, **358**, 124287, DOI: 10.1016/j.apcatb.2024.124287.

21 B. Baach, L. Boudad, I. Saber, M. Taibi and T. Guedira, Structural characterization and dielectric behavior of substituted bismuth niobate Bi17Nb3-4xV2xP2xO33 with fluorite-like structure, *Mater. Chem. Phys.*, 2024, **317**, 129201, DOI: 10.1016/j.matchemphys.2024.129201.

22 M. P. Bilibana, Electrochemical properties of MXenes and applications, *Adv. Sens. Energy Mater.*, 2023, **2**(4), 100080, DOI: 10.1016/j.asems.2023.100080.

23 Y. Liu, Y. Zhang, Z. Sun, L. Dai, B. Liu and W. Li, Catalysts with three-dimensional porous structure for electrocatalytic water splitting, *Sustainable Mater. Technol.*, 2025, **44**, e01392, DOI: 10.1016/j.susmat.2025.e01392.

24 H. Zhang, *et al.*, Highly ordered single crystalline nanowire array assembled three-dimensional NB32O7(OH) and Nb22O5 Superstructures for Energy Storage and Conversion Applications, *ACS Nano*, 2016, **10**(1), 507–514, DOI: 10.1021/acsnano.5b05441.

25 X. Wang, M. Yu and X. Feng, Electronic structure regulation of noble metal-free materials toward alkaline oxygen electrocatalysis, *eScience*, 2023, **3**(4), 100141, DOI: 10.1016/j.esci.2023.100141.

26 X. Wang, *et al.*, Importing Atomic Rare-Earth Sites to Activate Lattice Oxygen of Spinel Oxides for Electrocatalytic Oxygen Evolution, *Angew. Chem., Int. Ed.*, 2025, **64**, e202415306, DOI: 10.1002/anie.202415306.

27 S. Anantharaj and S. Noda, How properly are we interpreting the Tafel lines in energy conversion electrocatalysis?, *Mater. Today Energy*, 2022, **29**, 101123, DOI: 10.1016/j.mtener.2022.101123.

28 D. Knozowski, *et al.*, Plasma–enhanced chemical vapor deposition of Co3O4 thin films as a new approach for improving oxygen evolution activity, *Catal. Today*, 2025, **458**, 115374, DOI: 10.1016/j.cattod.2025.115374.

29 H. Wang, *et al.*, High-Valence Oxides for High Performance Oxygen Evolution Electrocatalysis, *Adv. Sci.*, 2023, **10**, 2301706, DOI: 10.1002/advs.202301706.

30 J. Feng, *et al.*, E-beam evaporated Nb2O5 as an effective electron transport layer for large flexible perovskite solar cells, *Nano Energy*, 2017, **36**, 1–8, DOI: 10.1016/j.nanoen.2017.04.010.

31 J. Ma, T. Zhang, J. Li, Y. Tian and C. Sun, Superhydrophilic/superaerophobic CoP/CoMoO4 multi-level hierarchitecture electrocatalyst for urea-assisted hydrogen evolution reaction in alkaline media, *J. Colloid Interface Sci.*, 2024, **669**, 43–52, DOI: 10.1016/j.jcis.2024.04.200.

32 A. Kazemi, F. Manteghi and Z. Tehrani, Metal Electrocatalysts for Hydrogen Production in Water Splitting, *ACS Omega*, 2024, **9**(7), 7310–7335, DOI: 10.1021/acsomega.3c07911.

33 S. Chu, *et al.*, Holey Ni-Cu phosphide nanosheets as a highly efficient and stable electrocatalyst for hydrogen evolution, *Appl. Catal., B*, 2019, **243**, 537–545, DOI: 10.1016/j.apcatb.2018.10.063.

34 L. Xu, *et al.*, Unveiling the mechanism of electrocatalytic oxidation of glycerol by in-situ electrochemical spectroscopy, *Chem. Eng. J.*, 2024, **481**, 148304, DOI: 10.1016/j.cej.2023.148304.

35 G. Pipitone, G. Zoppi, R. Pirone and S. Bensaid, A critical review on catalyst design for aqueous phase reforming, *Int. J. Hydrogen Energy*, 2022, **47**(1), 151–180, DOI: 10.1016/j.ijhydene.2021.09.206.

36 S. Jadeja, R. Kupcik, I. Fabrik, H. Sklenářová and J. Lenčo, A stationary phase with a positively charged surface allows for minimizing formic acid concentration in the mobile phase, enhancing electrospray ionization in LC-MS proteomic experiments, *Analyst*, 2023, **148**(23), 5980–5990, DOI: 10.1039/d3an01508d.

37 S. G. Nnabuife, A. K. Hamzat, J. Whidborne, B. Kuang and K. W. Jenkins, Integration of renewable energy sources in tandem with electrolysis: A technology review for green hydrogen production, *Int. J. Hydrogen Energy*, 2024, **107**, 218–240, DOI: 10.1016/j.ijhydene.2024.06.342.